ADVANCED FUNCTIONAL MATERIALS

Supporting Information

for *Adv. Funct. Mater.*, DOI: 10.1002/adfm.201706592

Development of Graphene Oxide/Polyaniline Inks for High Performance Flexible Microsupercapacitors via Extrusion Printing

Yuqing Liu, Binbin Zhang, Qun Xu, Yuyang Hou, Shayan Seyedin, Si Qin, Gordon G. Wallace, Stephen Beirne, Joselito M. Razal, and Jun Chen**

Supporting Information

Development of Graphene Oxide/Polyaniline Inks for High Performance Flexible Microsupercapacitors via Extrusion Printing

Yuqing Liu[1], Binbin Zhang[1], Qun Xu[2], Yuyang Hou[1], Shayan Seyedin[3], Si Qin[3], Gordon G. Wallace[1,], Stephen Beirne[1], Joselito M. Razal[3], and Jun Chen[1,]**

1. Characterization on printable inks and printed patterns

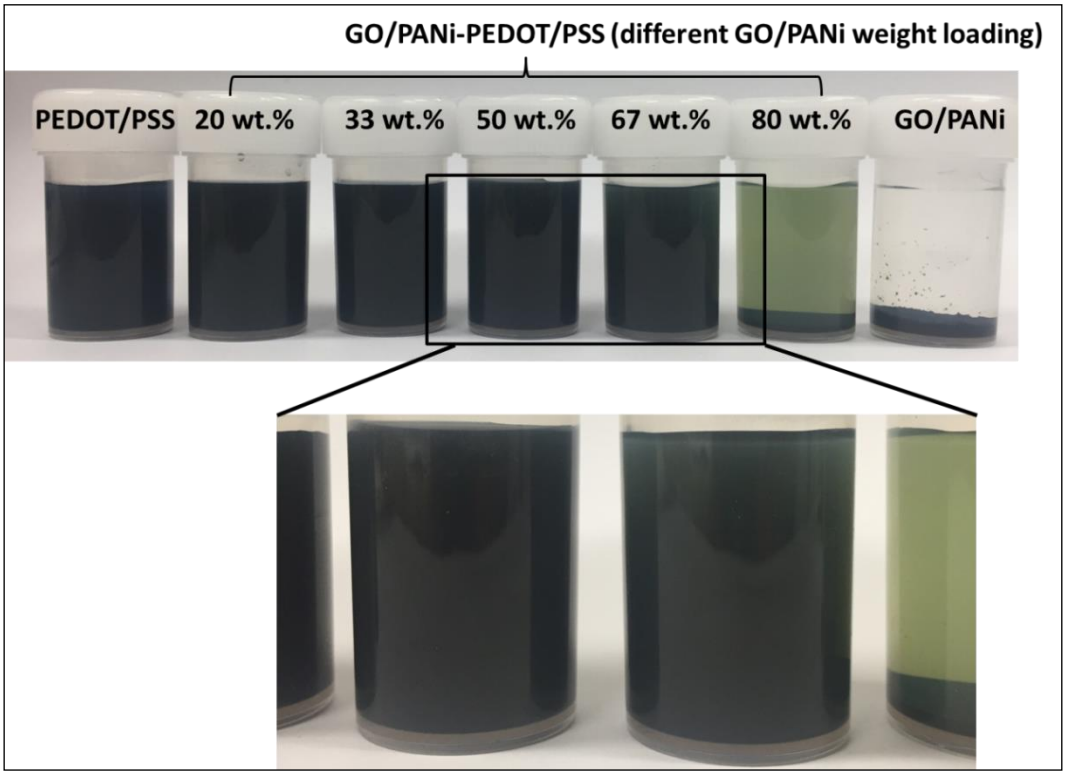

Figure S1. Digital photographs of GO/PA-PE dispersions with different GO/PANi loadings.

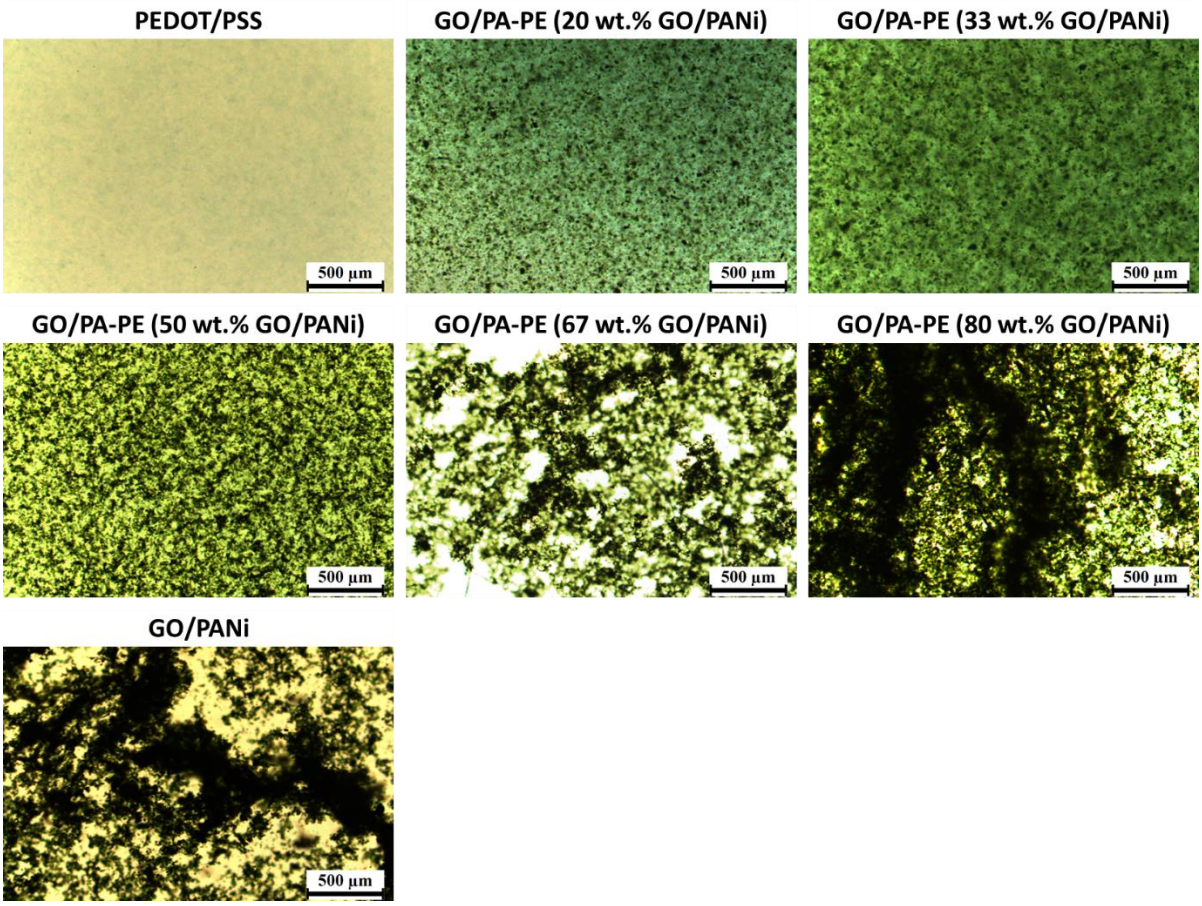

Figure S2. Optical microscopy images of the following dispersions: PEDOT/PSS, GO/PANi, and GO/PA-PE dispersions with different GO/PANi loadings.

The stability of the dispersions after being settled for one day was examined by optical microscopy in transmission mode. No obvious particles were observed in the PEDOT/PSS dispersion, indicating its excellent dispersibility in water (Figure S2). Small GO/PANi particles were uniformly distributed in GO/PA-PE dispersions with less than ~50 wt. % GO/PANi, while apparent aggregations of large particles were observed in dispersions with above ~50 wt. % GO/PANi loading.

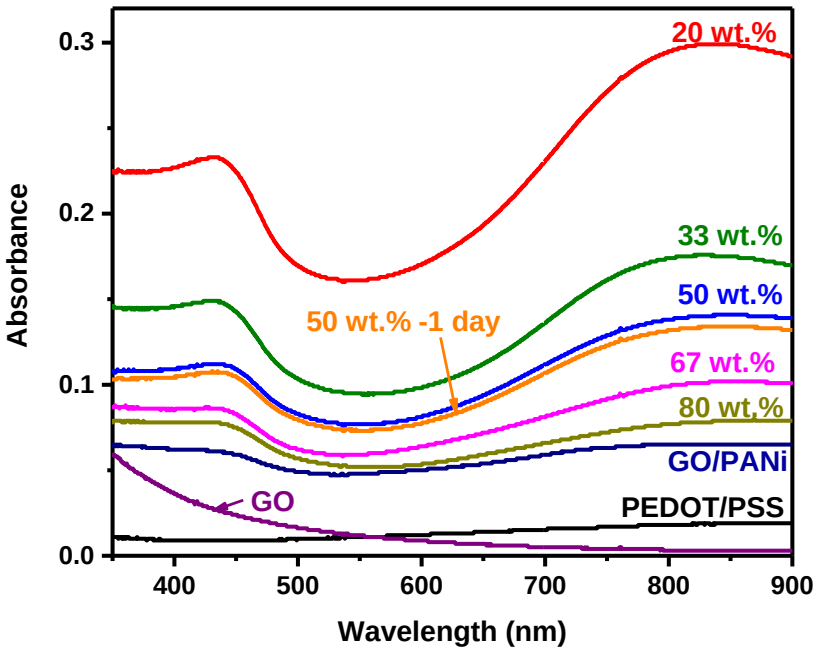

Figure S3. UV-vis spectra of PEDOT/PSS, GO/PA-PE, and GO/PANi dispersions.

The UV-vis spectra of the aqueous dispersions of all samples confirm the function of PEDOT/PSS as stabilizer (Figure S3). In the GO/PANi and all GO/PA-PE samples, two characteristic absorption bands at around 440 nm and 818 nm were observed, which correspond to the polaron-π* and π-polaron transitions in PANi, respectively.[1] While keeping the concentration of GO/PANi the same in all the GO/PA-PE dispersions, these peaks became more distinct with the increased amount of PEDOT/PSS, which indicate that more GO/PANi were distributed uniformly with the assistance of PEDOT/PSS. In addition, the spectrum of GO/PA-PE with 50 wt. % GO/PANi loading was almost unchanged after 1 day, demonstrating the excellent stability of the as-prepared inks.'

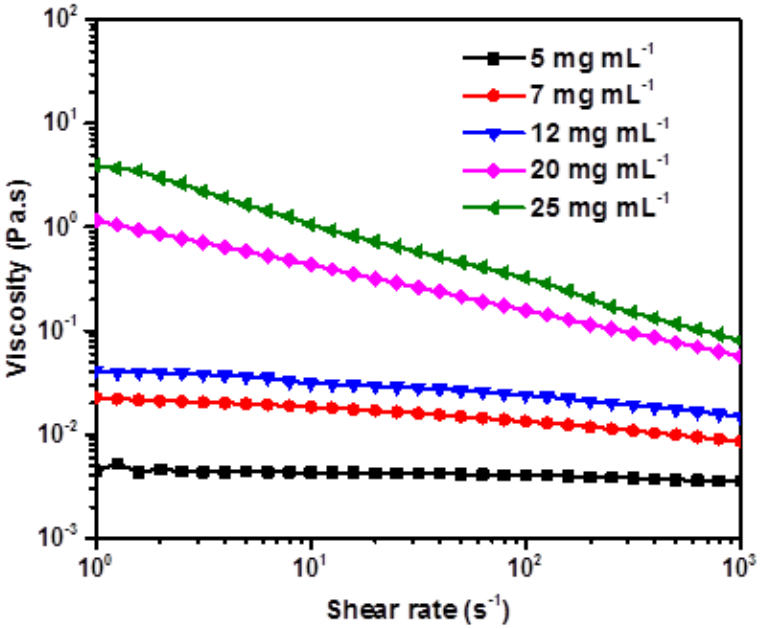

Figure S4. Viscosity of PEDOT:PSS dispersion with different concentration

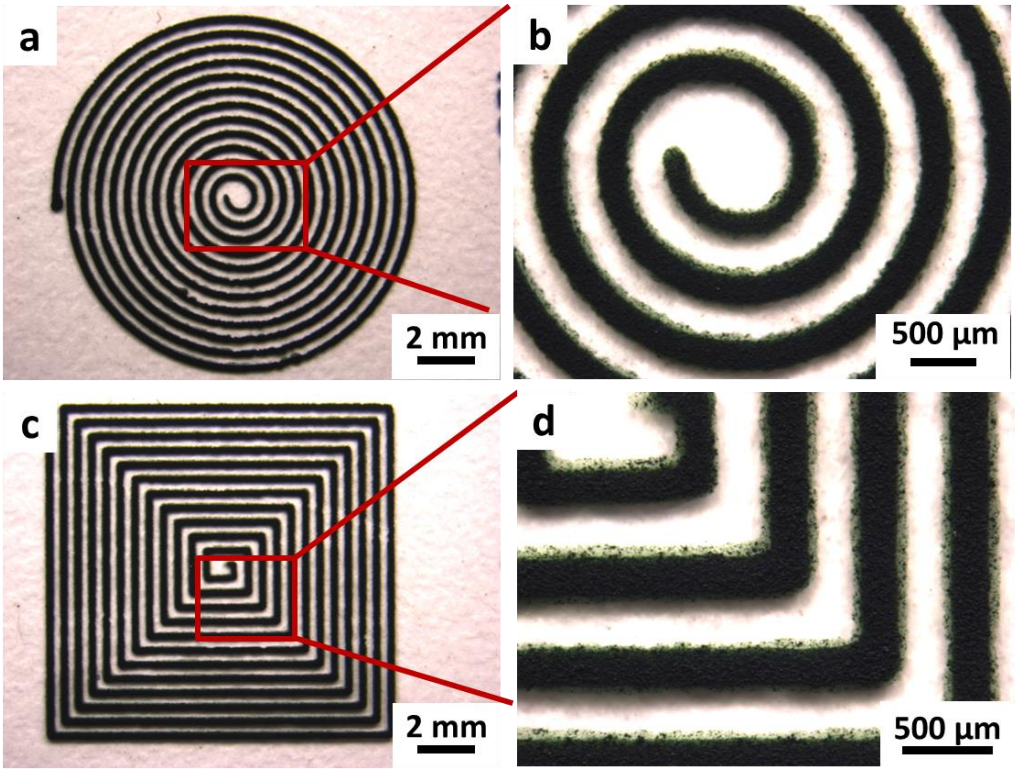

Figure S5. Optical microscopy images of printed GO/PA-PE antennas with curved and straight lines.

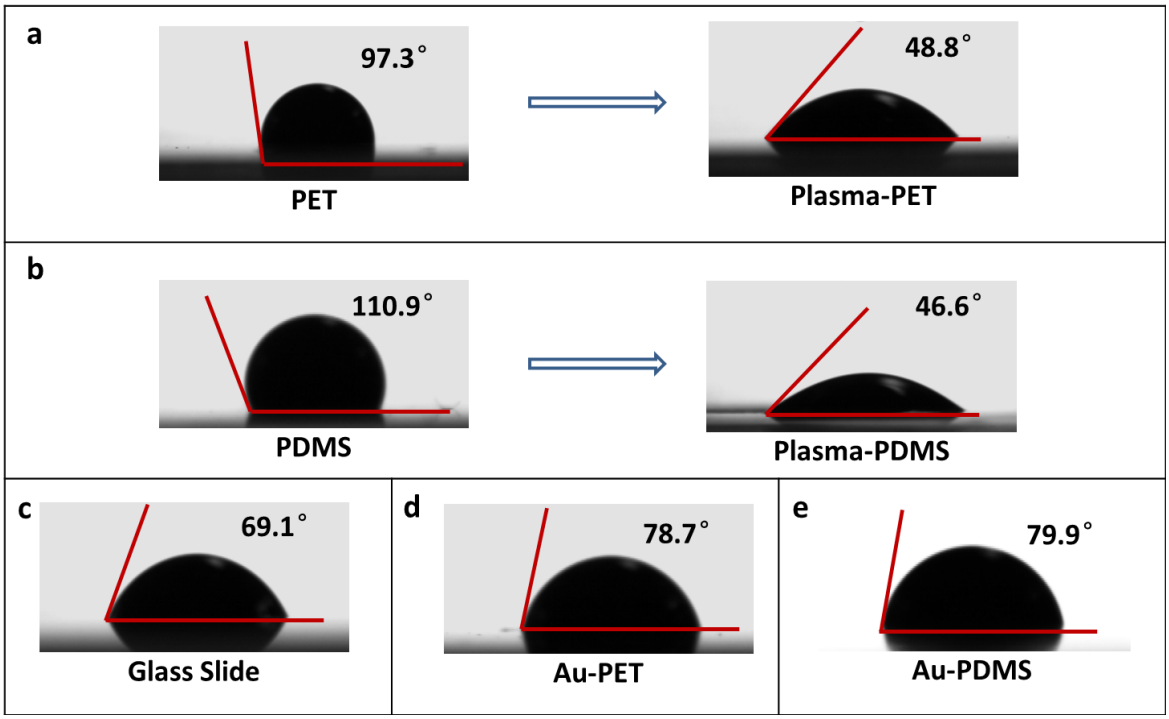

Figure S6. Contact angles between the GO/PA-PE ink and different substrates.

2. Characterizations of as-prepared samples

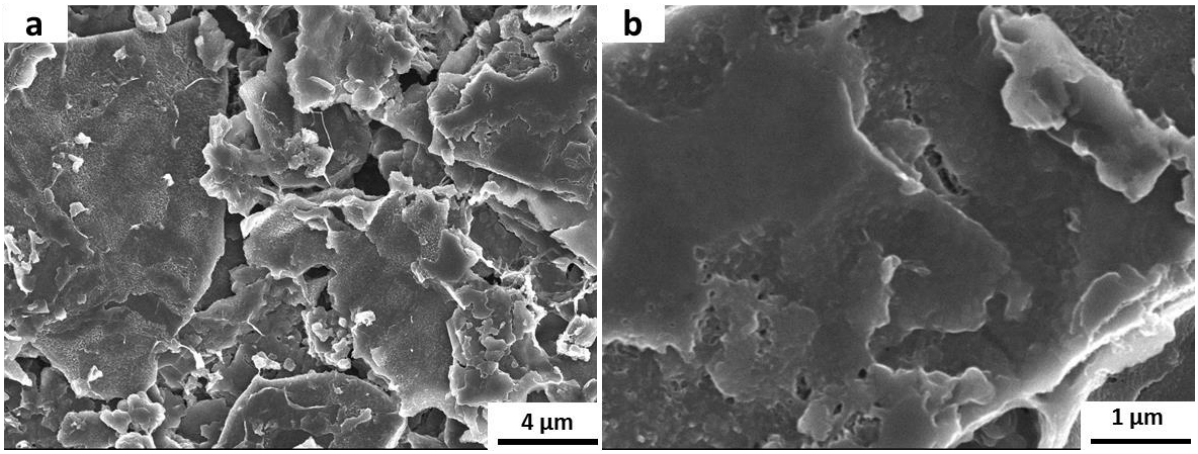

Figure S7. Top view SEM images of a typical printed GO/PA-PE pattern.

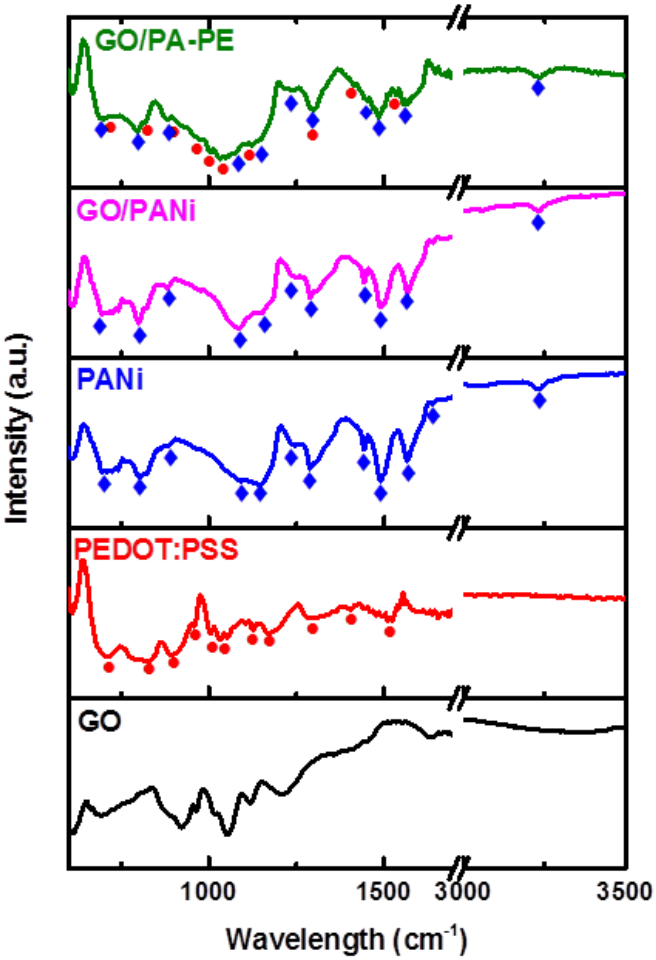

Figure S8. FTIR spectra of pure GO, pure PEDOT:PSS, pure PANi, GO/PANi and GO/PANi-PEDOT:PSS (GO/PA-PE) composites.

The FTIR spectra corroborated the Raman results. The PANi signature peaks[2] were observed in the GO/PANi and GO/PA-PE composites at 1568 cm^{-1} and 1490 cm^{-1} (stretching vibration bands of quinonoid and benzenoid rings, respectively), 1290 cm^{-1} (C-N stretching of secondary aromatic amines), and 1150 cm^{-1} (C-H of quinonoid ring) confirming the presence of PANi. All the PEDOT:PSS signature peaks[3] at 1167, 1126, 1029 cm^{-1} (related to S-O and S-phenyl bonds in sulfonic acid, respectively) and bands at 1580, 1508, 1001, 894, 771 and 706 cm^{-1} (corresponding to the C=C, C-C and C-S bonds in the thiophene backbone) were also observed in the GO/PA-PE composites. The peaks belonging to graphene oxide[4] at 1051 cm^{-1} (alkoxy), 1218 cm^{-1} (for epoxy), 1409 cm^{-1} (C-O in carboxy) were surpassed by the peaks of polymers and were not visible in the composite samples.

3. Viscosity of RGO-PE inks and the printed interdigitated microelectrodes

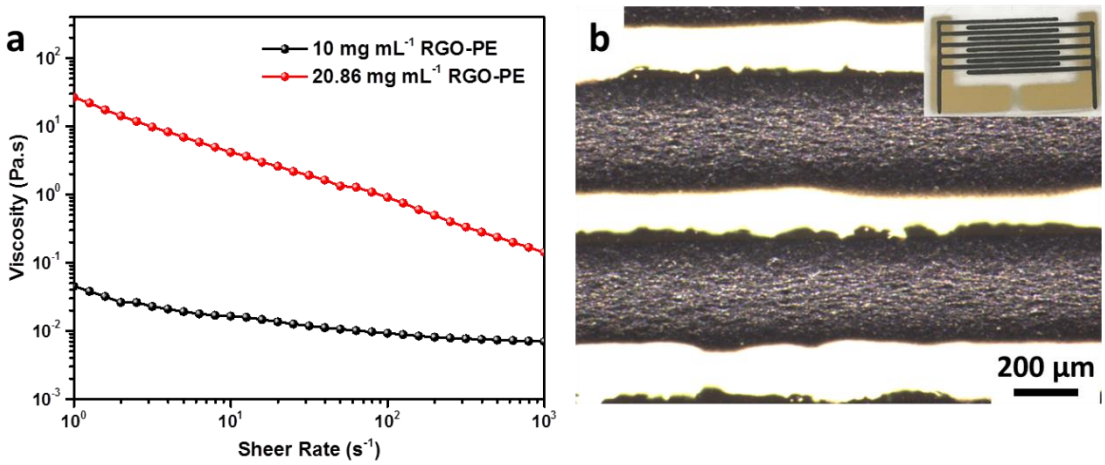

Figure S9. (a) Viscosity of RGO-PEDOT/PSS dispersion with different concentration and (b) optical microscope images of printed lines.

The viscosity of concentrated RGO-PE ink was also measured. A great increase in viscosity from 0.05 Pa•s to 30 Pa•s at 1 s^{-1} shear rate was achieved after concentrating the dispersion from ~10 mg mL^{-1} to ~21 mg mL^{-1}. The viscosity value for the RGO-PE ink was higher than the printable GO/PA-PE inks. The interdigitated microelectrode pattern was generated from the concentrated RGO-PE ink, which showed similar resolution to the GO/PA-PE patterns.

4. Dimensions and electrode loading in symmetric fMSC devices

Table S1. Dimensions of the symmetric fMSC patterns.

Symmetric fMSC		
Number of fingers each electrode	5	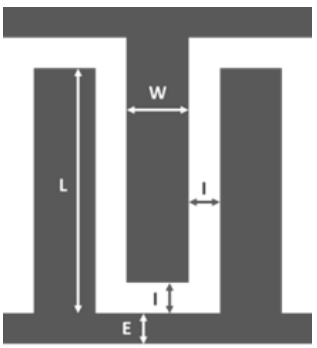
Width, W (µm)	350	
Interspace, I (µm)	150	
Length, L (µm)	8,000	
Edge, E (µm)	400	
Area of active materials (cm^2)	0.28	
Total projected area (cm^2)	0.4	

Table S2. Mass loading of active materials and electrode thickness for each device.

Name of fMSC	Mass per device (mg)	Mass per area (mg cm^{-2})	Thickness of electrode (µm)
GO/PA-PE (20 wt% GO/PANi)	0.1175	0.2938	4.5
GO/PA-PE (33 wt% GO/PANi)	0.1170	0.2925	4.5
GO/PA-PE (50 wt% GO/PANi)	0.1120	0.2800	4.6
RGO-PE (50 wt% GO)	0.0994	0.2486	4.0
PEDOT:PSS	0.0938	0.2344	5.0

5. Electrochemical performance of GO/PA-PE composite fMSCs with different GO/PANi loading

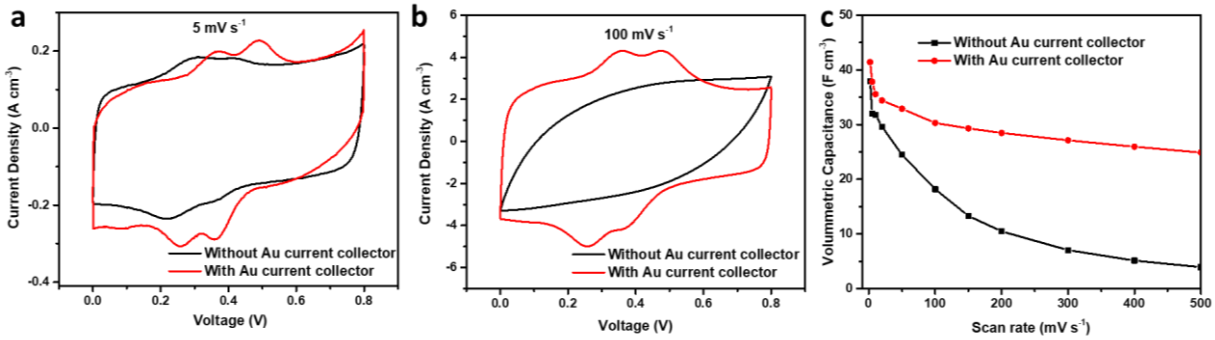

Figure S10. Comparison between devices with and without Au current collectors. (a) CV curves at 5 mV s^{-1}, (b) CV curves at 100 mV s^{-1}, and (c) volumetric capacitance calculated from CV curves at different scan rates.

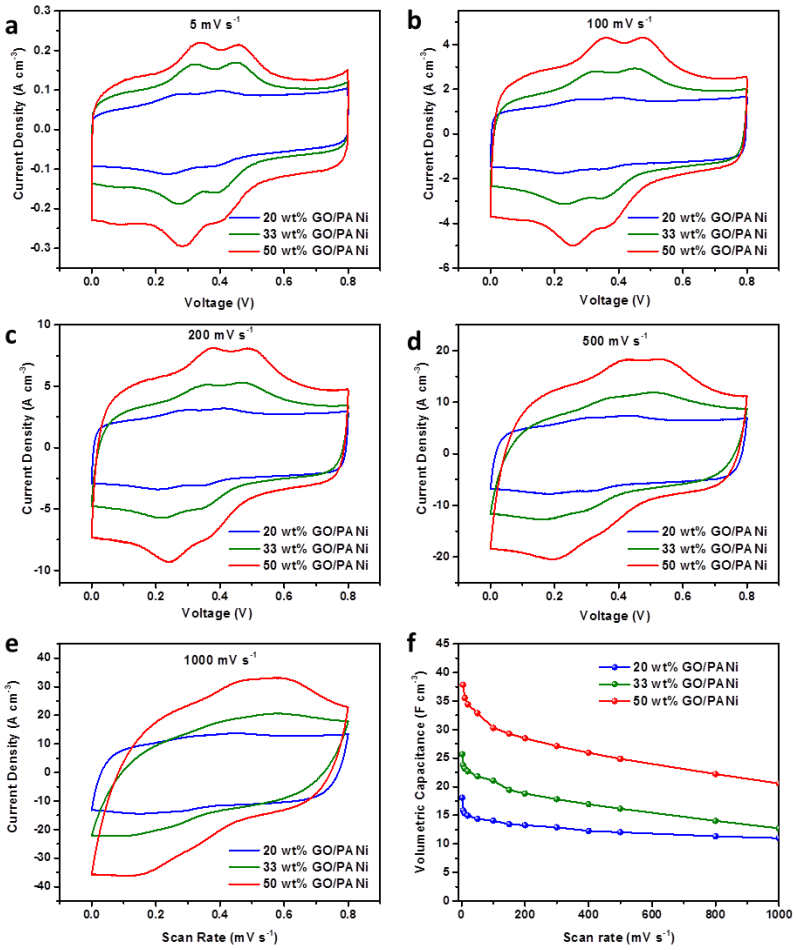

Figure S11. Comparing the electrochemical performance of fMSCs based on GO/PANi-PEDOT:PSS electrodes with different GO/PANi mass loadings.

6. The role of GO template

The GO component in the composite provides a robust supporting template for the aligned PANi nanorods, and consequently increases the capacitance of PANi. For comparison, pure PANi was prepared in the absence of GO in the aqueous phase using the same interfacial polymerization method. It is clearly seen in the SEM image that the vertically aligned nanorods are obtained when GO is used (Figure S12a), which are also considerably smaller in diameter than the randomly connected thicker PANi nanowires (Figure S12b) without the use of GO. This is because the GO template offers abundant nucleation sites for the growth of PANi.[5] The It can be deduced that the PANi component on GO provides an optimized ionic transport pathway and larger ion-accessible surface area, which can enhance the

capacitance.[5]To confirm the role of GO in the GO/PA-PE device, fMSCs based on PEDOT:PSS, GO-PEDOT:PSS (GO-PE, 50 wt. % GO loading), PANi-PEDOT:PSS (PA-PE, 50 wt. % PANi loading), and GO/PA-PE (50 wt. % GO/PANi loading) were prepared following our previously reported laser-etching method.[6] The GO-PE and PA-PE formulations were prepared by simply mixing GO and PANi with PEDOT/PSS. The mass loading of the parent film before etching was 2 mg cm-2 in all fMSCs. The GO/PA-PE fMSC exhibited highest capacitance and best rate capability performance compared to all other devices (Figure S13). Notably, the GO-PE fMSC exhibited lower capacitance than the PEDOT:PSS fMSC. Therefore, the GO component serves as a template for PANi growth with very minimal contribution to the capacitance.In addition, the electrical conductivity of the printed GO/PA-PE lines (width ~ 800 µm and thickness ~ 10 µm) was measured as 64.01 S cm^{-1} which was higher than that of PA-PE (~59.04 S cm^{-1}), and much higher than that GO-PE lines (~6.10 S cm^{-1}), despite the use of insulating GO in the GO/PA-PE composite. This is because of the very small amount of GO in the GO/PANi composite, the polymerization feeding ratio of GO:aniline is 1:19. This ratio ensured that all GO sheets were covered by conductive PANi nanorods and thick PANi nanowires did not grow. This can also explain why water dispersible GO in GO/PA-PE did not stabilize PANi in water because its functional groups were covered by PANi.

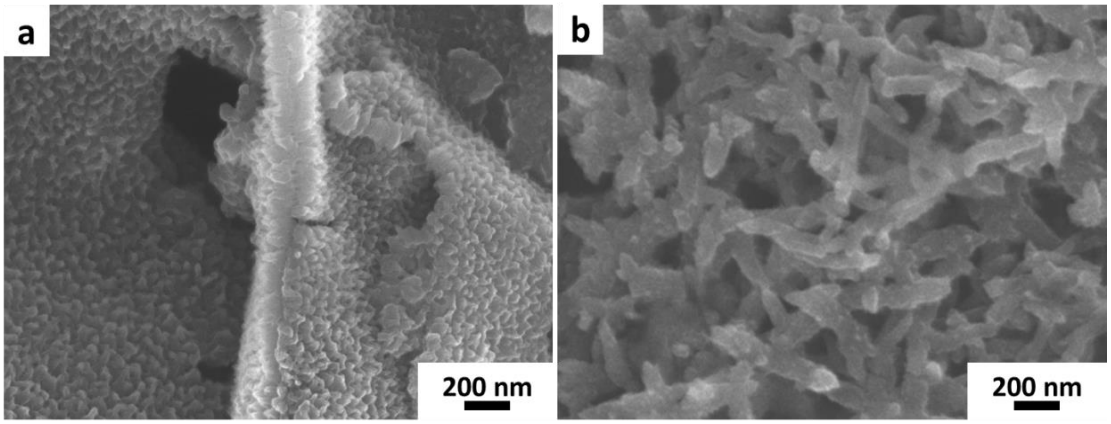

Figure S12. Comparison of SEM images between (a) GO/PANi composite and (b) PANi nanowires.

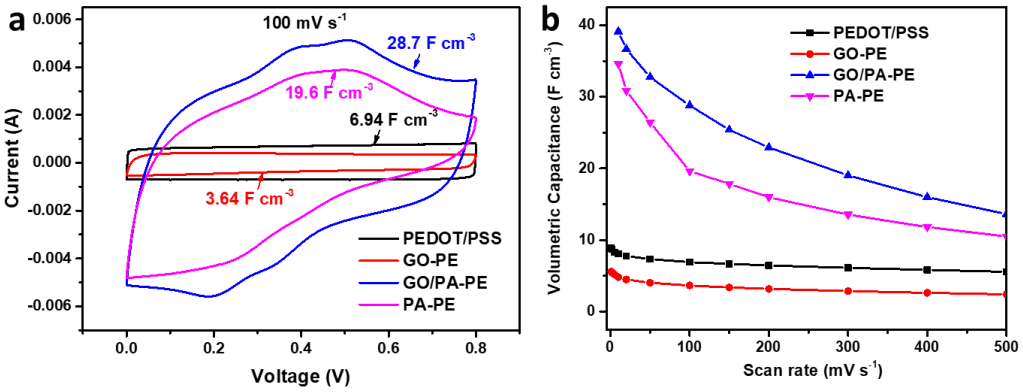

Figure S13. Comparison of the electrochemical performance of PEDOT/PSS, GO-PE, GO/PA-PE and PA-PE fMSCs. (a) CV curves at the scan rate of 100 mV s^{-1}, and (b) volumetric capacitance calculated from the CV curves at various scan rates.

7. CV curves of optimized GO/PA-PE fMSC

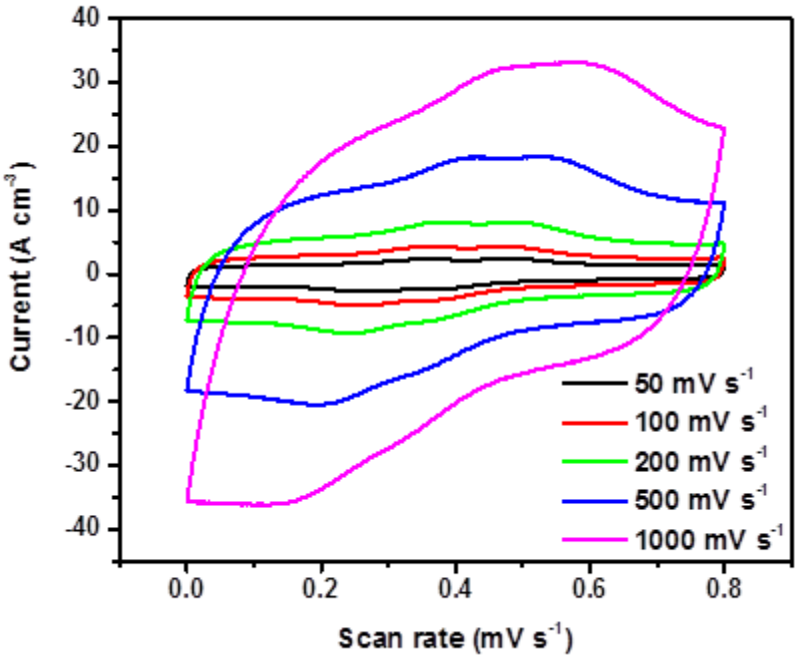

Figure S14. CV curves of GO/PA-PE fMSCs (50 wt.% GO/PANi loading) at different scan rates.

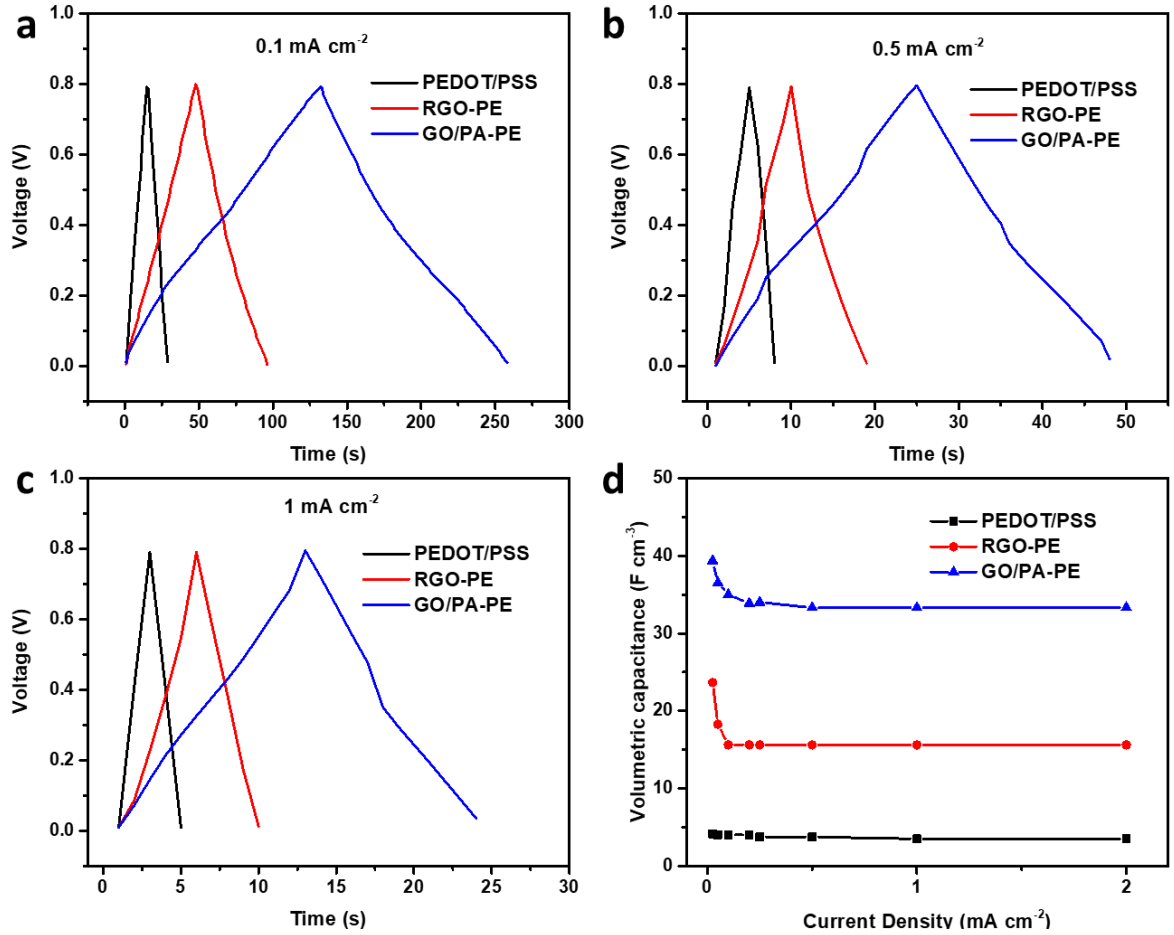

Figure S15. Comparison of the GCD curves of the GO/PA-PE fMSC with PEDOT/PSS and RGO-PE fMSCs at the current density of (a) 0.1 mA cm^{-2}, (b) 0.5 mA cm^{-2}, (c) 1 mA cm^{-2}. (d) Volumetric capacitance of the fMSCs calculated at different current densities.

The GCD curves of GO/PA-PE fMSC clearly showed longer discharge time than the pure PEDOT/PSS and RGO-PE fMSCs at all constant discharge currents, indicating its higher capacitance and its excellent rate capability. The symmetric charge-discharge curves and minimal iR drop at the beginning of the constant current discharge suggest good capacitive behavior and low contact resistance of the GO/PA-PE fMSC device.

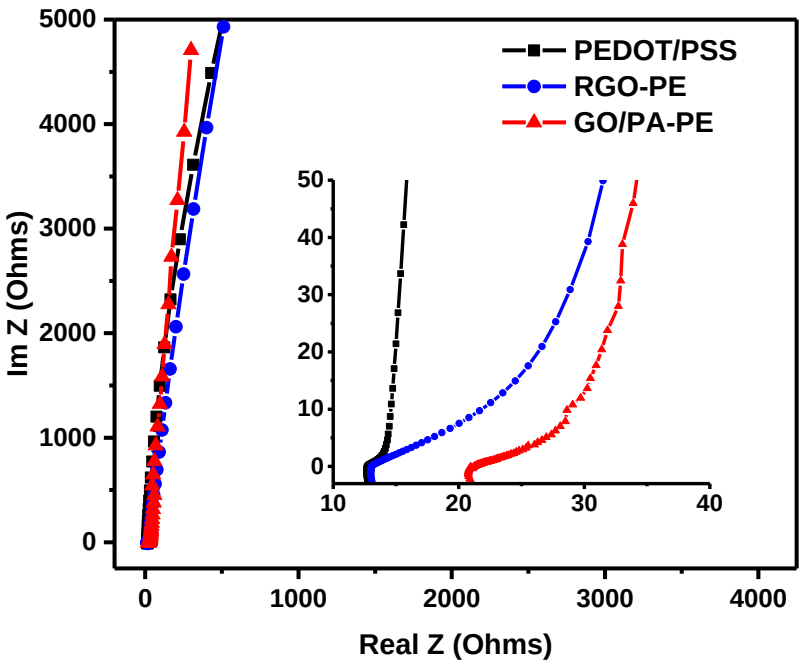

Figure S16. Nyquist plots for PEDOT/PSS, RGO-PE, and GO/PA-PE fMSCs.

The small charge transport resistance (R_{ct}, derived from the radius of the semi-circle at high frequency region) and the high slop of the vertical line in the low frequency region of the Nyquist plots (Figure S16) suggest fast ion-diffusion rate and good capacitive behavior for the GO/PA-PE fMSC, although the GO/PA-PE fMSC exhibitS larger equivalent series resistance (ESR, defined by the intercept of the real part of impedance with the x-axis) than the RGO-PE and PEDOT/PSS device.

8. Characterization of fMSCs with different printing layers

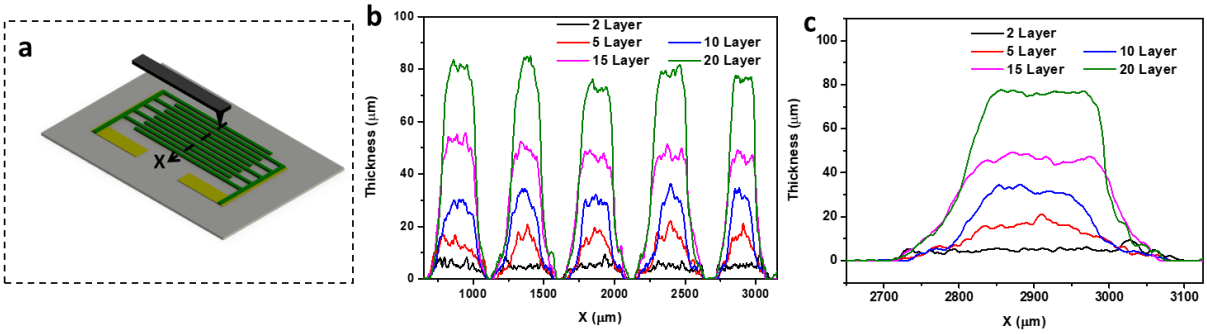

Figure S17. (a) Schematic illustration of thickness measurements via Dektak profilometer. (b) Thickness profiles of fMSCs with different printed layers. (c) enlarged thickness profile of an electrode finger.

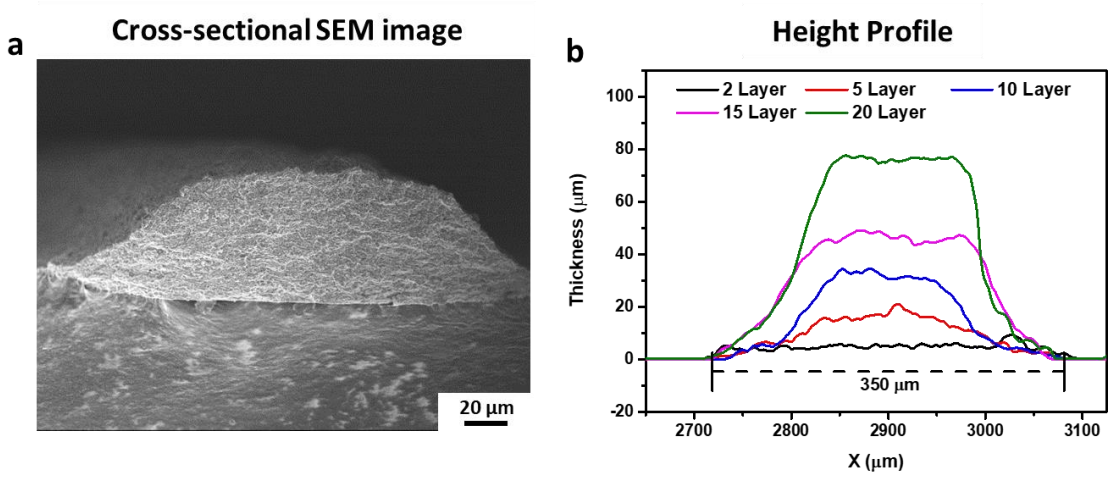

Figure S18. (a) Cross-sectional SEM images and (b) thickness profile of a 20-layer printed electrode finger.

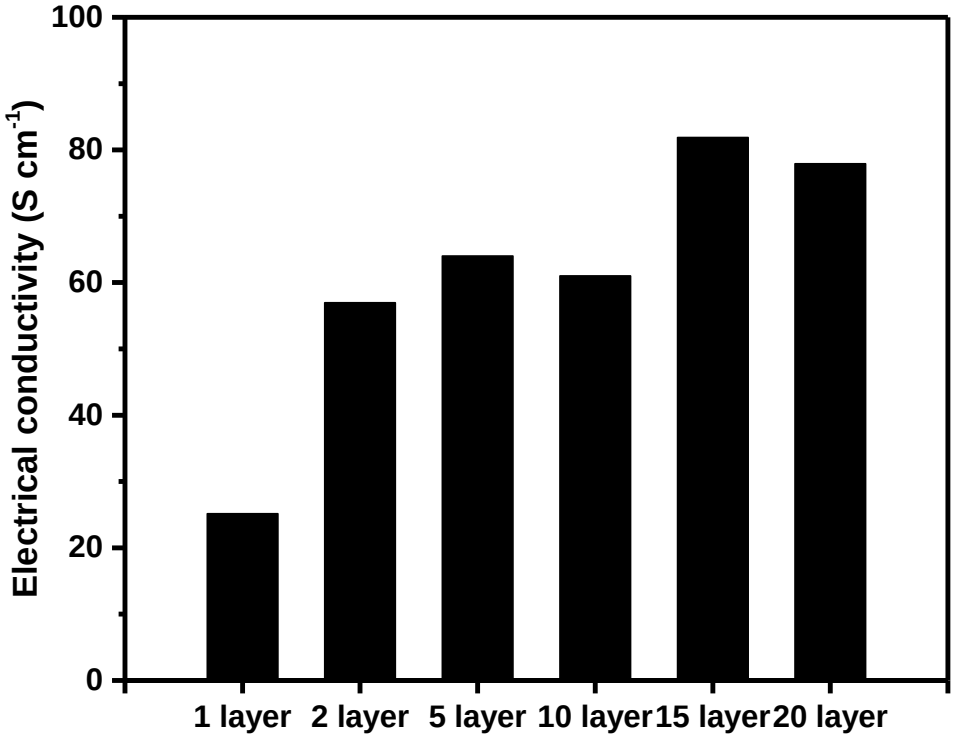

Figure S19. Electrical conductivity of GO/PA-PE electrodes with various printing layers.

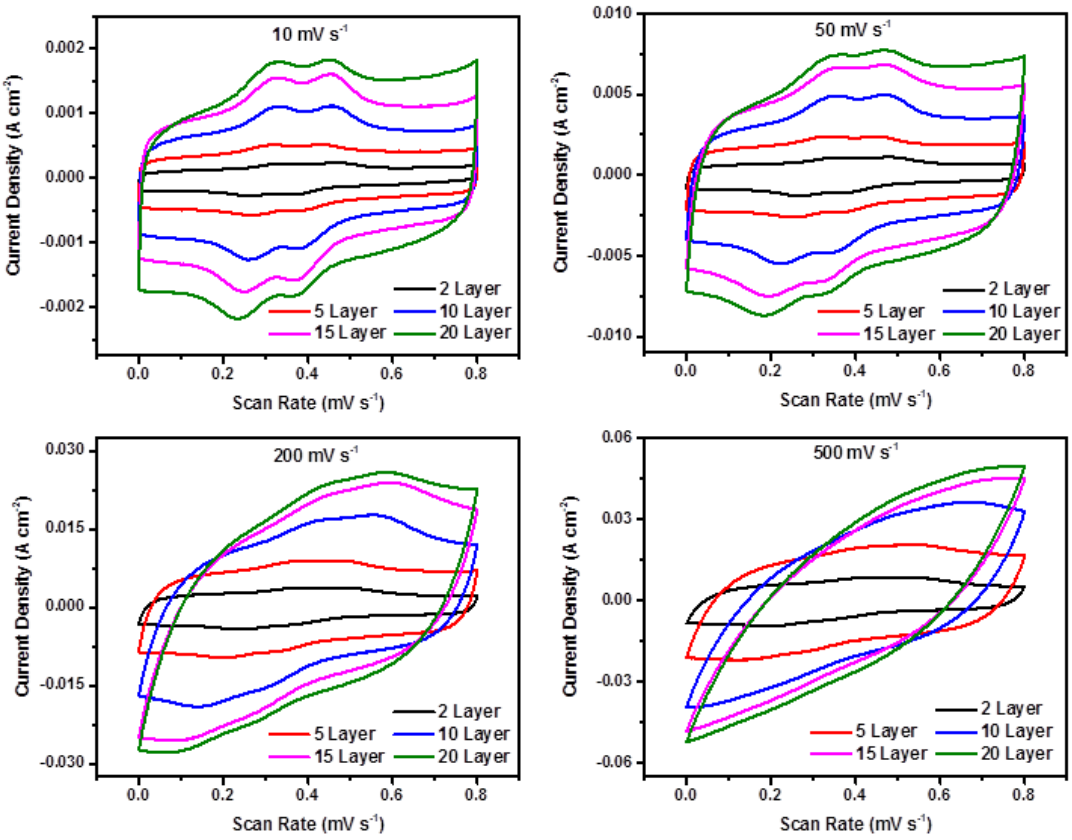

Figure S20. CV curves of fMSCs with different printed layers at different scan rates.

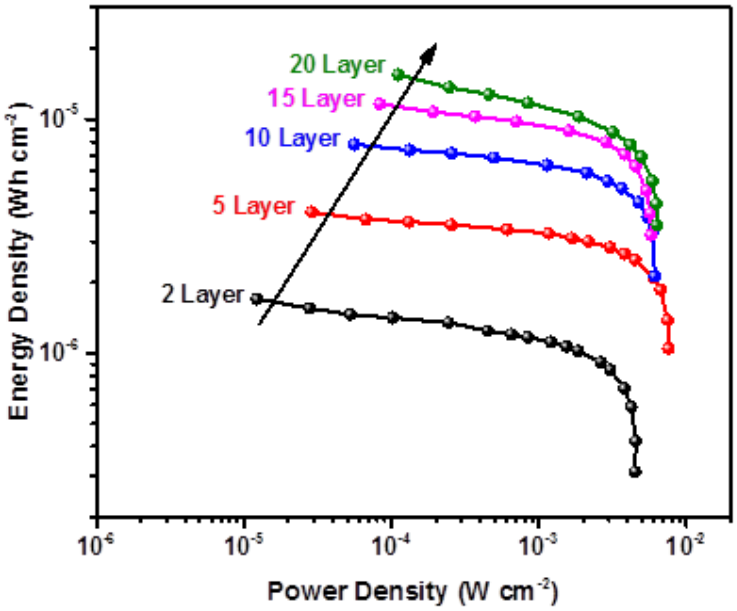

Figure S21. Ragone plot of fMSCs with different printed layers.

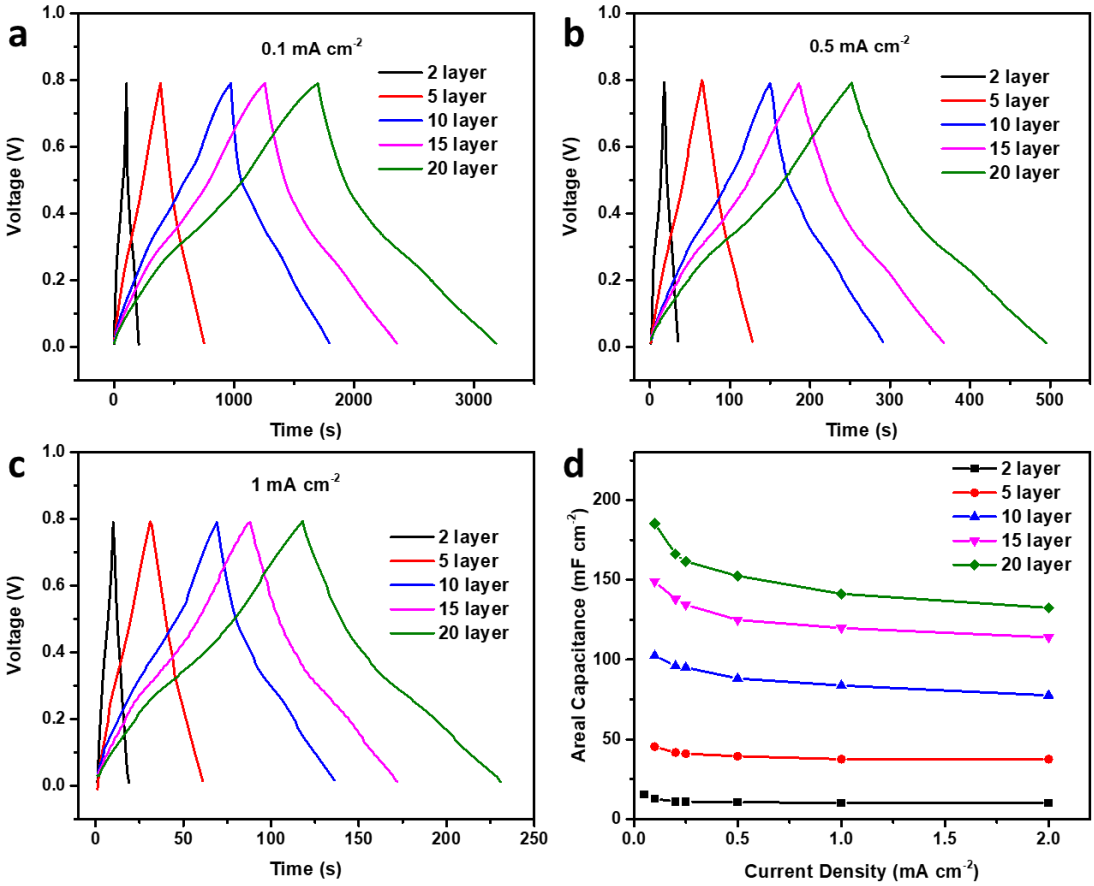

Figure S22. GCD curves of GO/PA-PE fMSCs with different printing layers at various current densities of (a) 0.1 mA cm^{-2}, (b) 0.5 mA cm^{-2}, and (c) 1 mA cm^{-2}.(d) calculated capacitance versus current densities.

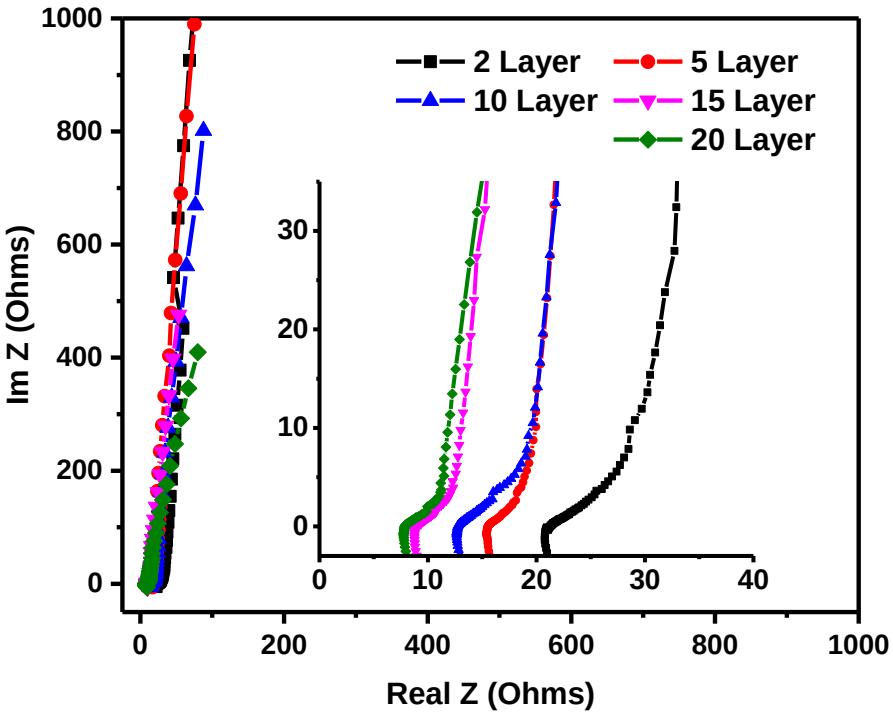

Figure S23. Nyquist plots of fMSCs with different printing layers.

'The Nyquist plot of fMSCs with different printed layers, showed high slope for the low-frequency region and small Rct in the high frequency part region for all devices, indicating their excellent capacitive behaviours (Figure S23). ESR also decreased from 21.3 Ω to 7.89 Ω when printing layers increased from 2 to 20. These observations are different in contrast with the previous reports on supercapacitors with sandwiched design[7], where the low-frequency slope decreased, and Rct and ESR increased sharply with electrode thickness. This is because in interdigitated design, the electrolyte ions could penetrate and diffuse along the parallel direction of the layered electrode materials as opposed to being limited to just the vertical direction in the conventional sandwiched design. Consequently, the ion accessible surface of electrode materials and ion transport length are not affected by the electrode thickness in interdigitated design. Meanwhile, the electron can also transport along the parallel direction in interdigitated design, hence the ESR becomes smaller for the thicker electrode due to the larger cross-section area (A) of the electrode (according to R=ρl/A, where R is electrical

resistance, ρ is electrical resistivity, and l is the length of the electrode). The larger electrical conductivity with increasing printing layers also account for the smaller ESR (Figure S19).'

9. Performance comparison between fMSCs with sandwiched and interdigitated designs

Table S3. Detailed comparison of the dimensions of sandwiched and interdigitated fMSCs.

Parameters		Sandwiched fMSC	Interdigitated fMSC
Device parameters	Active materials loading of device	2.8 mg cm^{-2}	2.8 mg cm^{-2}
	Mass of active materials	1.12 mg	1.12 mg
	Size of device	0.8 cm × 0.5 cm	0.8 cm × 0.5 cm
	Device thickness	112 μm	80.2 μm
Each electrode parameters	Electrode mass	0.56 mg	0.56 mg
	Electrode thickness	9.48 μm	80 μm
	Electrode footprint area	0.4 cm^2	0.14 cm^2

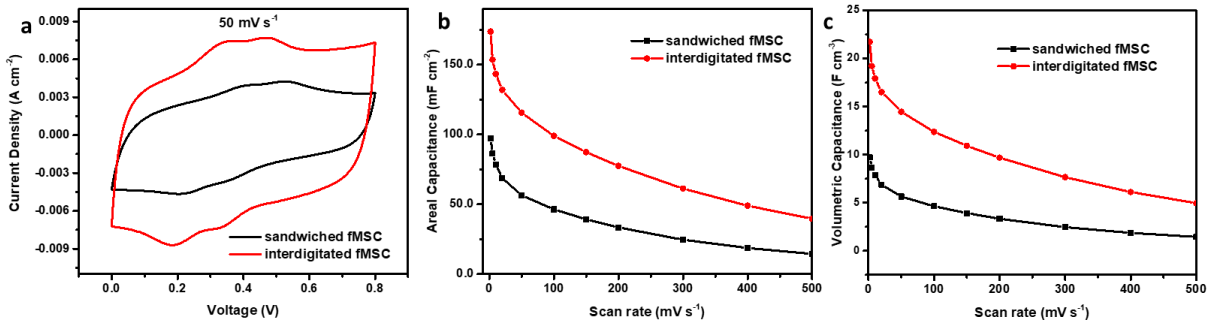

Figure S24. Performance comparison between fMSCs with sandwiched and interdigitated designs. (a) CV curves at 50 mV s^{-1}, (b) areal capacitance, and (c) volumetric capacitance.

10. Asymmetric design

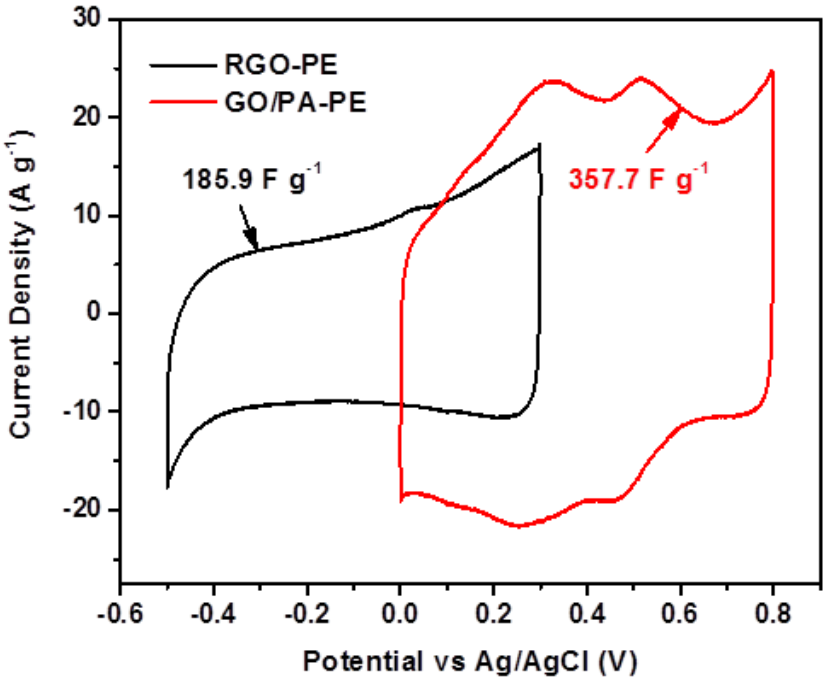

Figure S25. CV curves (100 mV s^{-1}) of RGO-PE and GO/PA-PE electrodes tested in three electrode system in 1 M H_2SO_4.

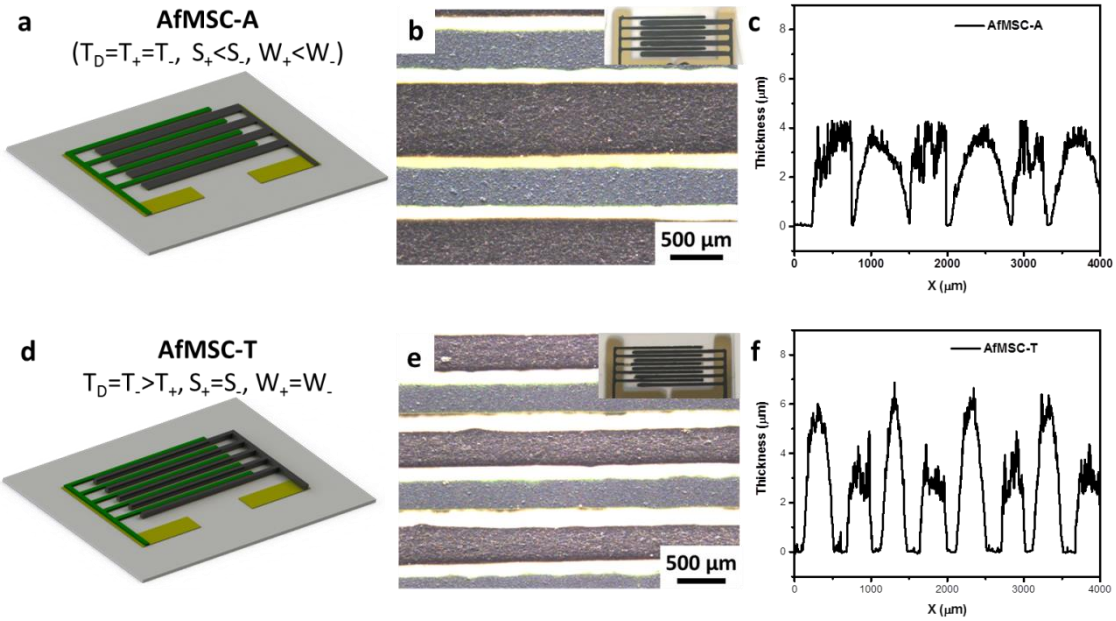

Figure S26. (a,d) Schematic illustration, (b,e) optical images and digital photographs, and (c,f) thickness of AfMSC-T and AfMSC-A devices.

In asymmetric supercapacitors, the electrode mass loadings in positive and negative electrodes are different to keep the charge balance. This would inevitably cause volume differences between the two electrodes. The volume difference can be achieved by varying either electrode thickness or the electrode foot-print area, and the former method was employed in most supercapacitors including sandwiched and interdigitated designs. It is reasonable in sandwiched supercapacitors where the two film electrodes that face each other possess the same area. However, in supercapacitors with interdigitated electrodes, there would be space wasted above the thin electrodes. In this case, the volume of the total device would be increased, which is not desirable considering fMSCs applications in microelectronics. Here, we used a better design which achieved the weight ratio balance of the two electrodes by varying the footprint area and thus keeping the electrode thickness constant.

The mass density of the two electrode materials was measured to be ~1.46 g cm^{-3} and ~1.40 g cm^{-3} for GO/PA-PE and RGO-PE respectively. Based on Equation S12, the area ratio was calculated to be $A_+/A_-=2.01 \approx 2$, which would be realized by varying the width of interdigitated fingers (Figure S17 a-c) during printing. The thickness of the extrusion printed asymmetric interdigitated microelectrodes was measured to be constant at 3.6 μm and the device was named as AfMSC-T (2 layer GO/PA-PE and 4 layer RGO-PE printed). Another asymmetric device (AfMSC-A) with device thickness of 6 μm which utilizes the traditional design (*i.e.* keeping area the same while varying electrode thickness) was also printed for comparison (1 layer GO/PA-PE printed and 6 layer RGO-PE printed). Having the same active materials mass loading, the two devices exhibited similar CV curves, indicating the same device capacitance (Figure S18a). However, when comparing the volumetric capacitance, the AfMSC-A showed a superior performance originated from the optimized space arrangement of electrodes, since device AfMSC-T is larger than device AfMSC-A. (Figure S18b).

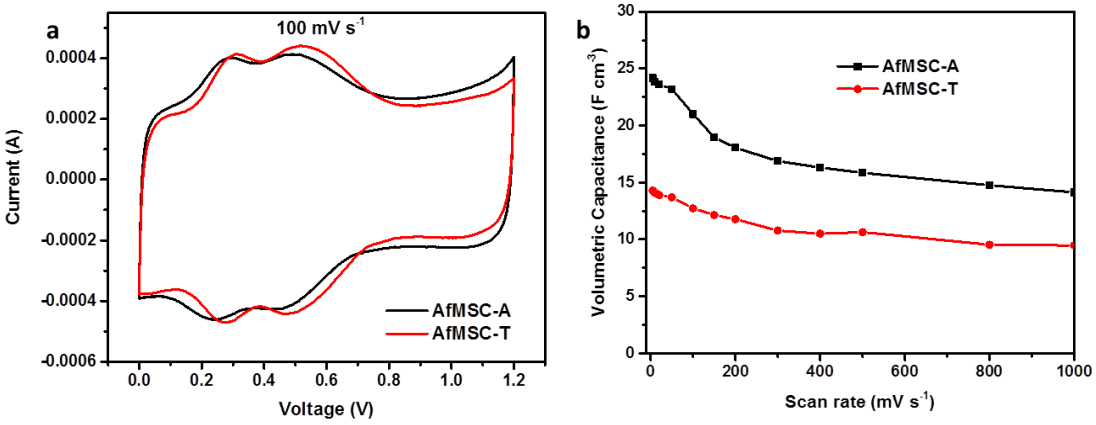

Figure S27. Performance comparison of AfMSC-A and AfMSC-T.

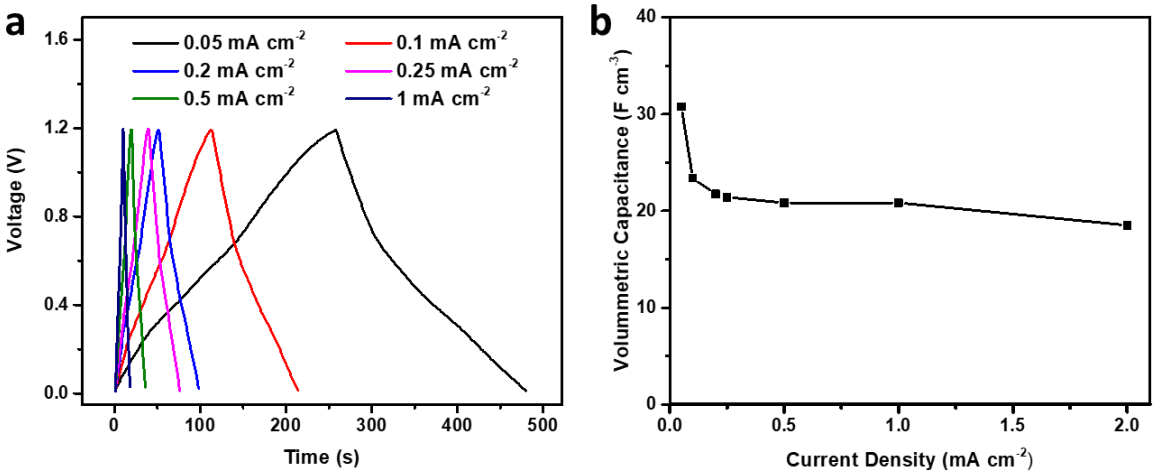

Figure S28. (a) GCD curves and (b) volumetric capacitance of the AfMSC measured from the GCD curves at different current densities.

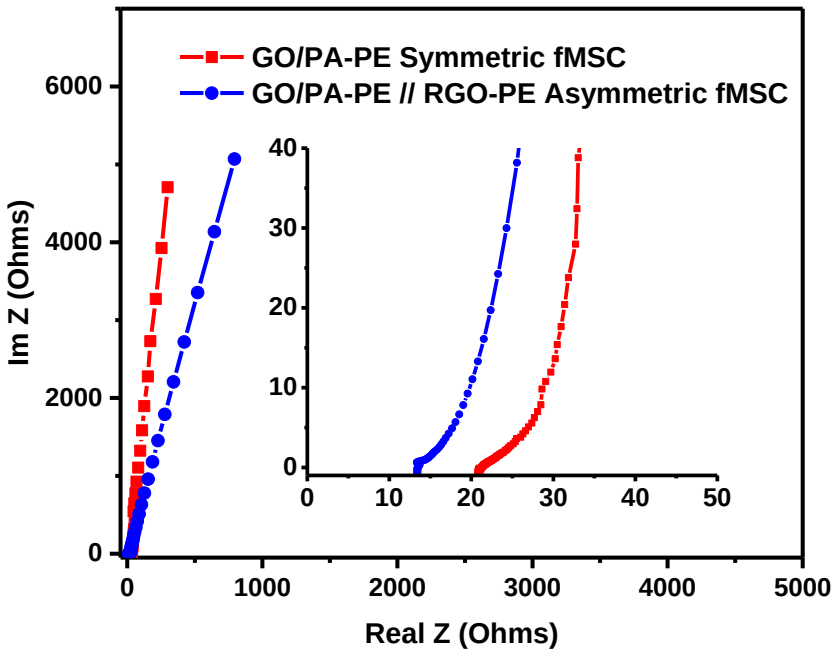

Figure S29. Nyquist plot of symmetric and asymmetric fMSCs.

The improvement in rate capability of asymmetric fMSC can also be explained by the impedance analysis of the Nyquist plot. In Figure S29, the asymmetric fMSC shows small ESR and R_{ct} in the high frequency region and a vertical slope in the low frequency region, which are the characteristics of the good capacitive behaviour and fast ion-transport rate. Specifically, the ESR of the asymmetric fMSC (14 Ω) is smaller than that of GO/PA-PE symmetric fMSC (21 Ω) due to the use of more conductive RGO-PE in the asymmetric fMSCs. The slightly larger Rct of the asymmetric device as displayed by the small semi-circle in the high-frequency part and the small reduction in slope in the low-frequency region can be explained by the increase in electrode finger width where the ion-transport between electrodes becomes longer.'

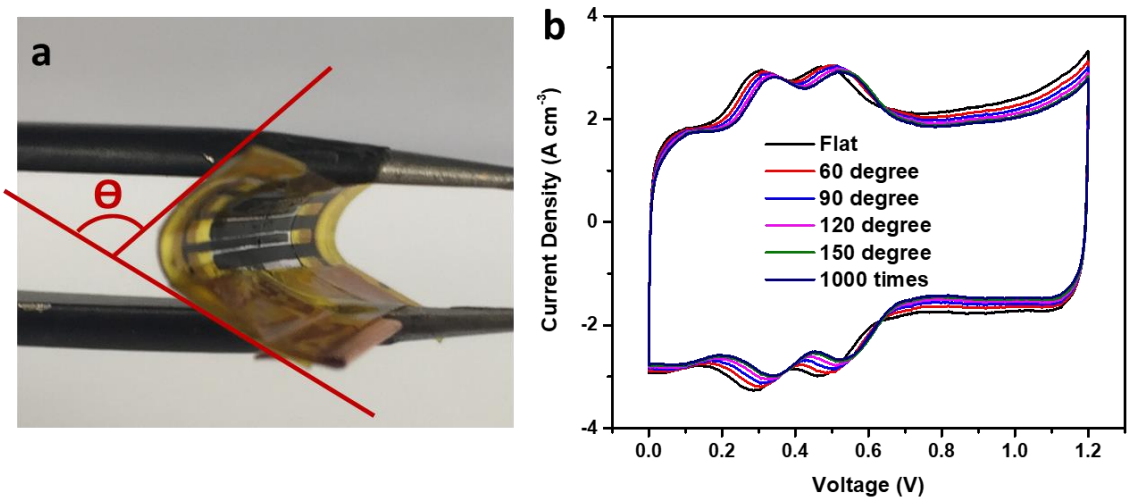

Figure S30. (a) Photograph of the AfMSC device at the bent state. (b) Comparison of the CV curve of the device before and after bending at different conditions. Also shown is the CV curve after repeated bending of the AfMSC device at 150 ° for 1000 times. Testing was performed at the scan rate of 100 mV s^{-1}.

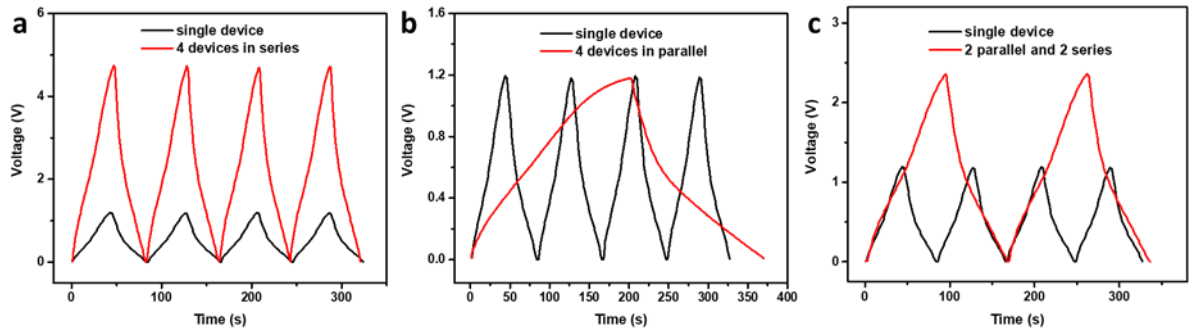

Figure S31. GCD curves (current density = 0.25 mA cm-2) of four fMSC devices connected in (a) series, (b) parallel, and (c) combination of series and parallel.

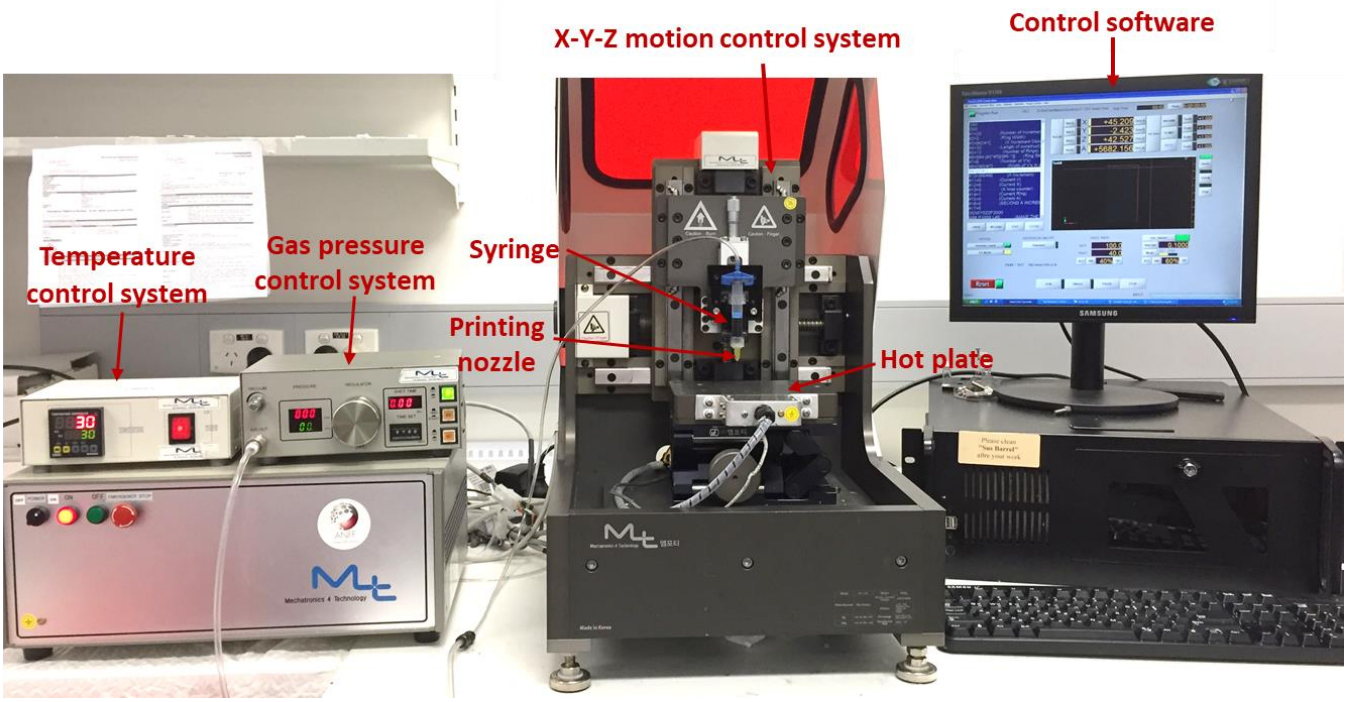

Figure S32. Photograph of the extrusion printing system.

11. Calculations

Bragg's Law (Equation S1) was used to calculate the interspace between graphene layers, where d is the inter-layer spacing, n=1, and λ is the wavelength of the incident wave (1.54 Å).

$$2d \sin\theta = n\lambda \quad \text{(S1)}$$

Device capacitance was calculated from CV curves and charge-discharge curves according to Equation S2 and S3, respectively. In these equations, $\int IdV$ is the integrated area of the CV curve, U is the voltage window (V), S is the scan rate (V s^{-1}), I_d is constant current used for charging and discharging (A), and ΔT_d is the discharge time (s).

$$C = \frac{\int I\, dV}{2 \times U \times S} \quad \text{(S2)}$$

$$C = \frac{I_d \times \Delta T_d}{U} \quad \text{(S3)}$$

Specific capacitance of the whole device was calculated according to Equation S4 and S5, where CA (in F cm^{-2}) and CV (in F cm^{-3}) refer to the areal capacitance and volumetric capacitance of the whole device, respectively, AD is the total projected area of the devices (1 cm^2) including the area of active materials and gaps between the microelectrodes, d (cm) is the thickness of the device including thickness of both the active material (T) and the current collector (100 nm).

$$C_A = \frac{C}{A_D} \tag{S4}$$

$$C_V = \frac{C_A}{d} \tag{S5}$$

Specific capacitance of electrode materials was calculated according to Equation S6 and S7, where $C_{A,\ electrode}$ (in F cm^{-2}) and $C_{V,\ electrode}$ (in F cm^{-3}) refer to the areal capacitance and volumetric capacitance of electrode materials, respectively, A_E is the area of active materials (not including gaps between the microelectrodes), T (cm) is the thickness of the electrode film.

$$C_{A,electrode} = \frac{C}{A_E} \tag{S6}$$

$$C_{V,electrode} = \frac{C_{A,electrode}}{T} \tag{S7}$$

Energy density and power density of the whole device were calculated from Equation S8 and S9, Where E is the energy density (Wh cm^{-2} or Wh cm^{-3}) and P is the power density (W cm^{-2} or W cm^{-3})

$$E = \frac{1}{2 \times 3600} \times (C_A \ or \ C_V) \times U^2 \tag{S8}$$

$$P = \frac{3600 \times E}{\Delta T_d} = \frac{3600 \times E}{\frac{U}{S}} \quad \text{(S9)}$$

Equation S10 and S11 were used to calculate the mass ratio of positive and negative electrodes in asymmetric design, while the occupying area ratio of the two electrodes was calculated from Equation S12. *m* is the mass of active materials, *C* is the gravimetric capacitance, Δ*E* is the stable voltage window, and *A*, *T*, *V*, and *D* are the footprint area, thickness, volume and mass density of active materials, respectively. The subscripts + and – represent the positive and negative electrode materials respectively.

$$\mathrm{q} = \mathrm{C} \times \mathrm{m} \times \Delta\mathrm{E} \quad \text{(S10)}$$

$$\frac{m_+}{m_-} = \frac{C_+ \Delta E_-}{C_+ \Delta E_-} \quad \text{(S11)}$$

$$\frac{A_+}{A_-} = \frac{\frac{V_+}{T}}{\frac{V_-}{T}} = \frac{V_+}{V_-} = \frac{\frac{m_+}{D_-}}{\frac{m_-}{D_-}} = \frac{m_+}{m_-} \times \frac{D_+}{D_-} \quad \text{(S12)}$$

Table S4. Comparison of electrochemical performances of various fMSCs.

Materials[a]	Electrolyte	Thickness of film (μm)	Areal Capacitance[b] (mF cm^{-2})	Volumetric Capacitance[c] (F cm^{-3})	Cycle life	Energy Density[d] (μWh cm^{-2})	Energy Density[e] (mWh cm^{-3})	Dimension[f] (μm)	Patterning technique
BNG[8]	PVA/H_2SO_4 (0~1 V)	0.008	0.0976 (10 mV s^{-1})*	~25.6 (10 mV s^{-1})*	95.2%, 100,000 cycles	0.0135*	3.4	W:210, I:70	oxygen plasma etching via mask
RGO[9]	PVA/H_3PO_4 (0~1 V)	0.025	0.462 (1 A g^{-1})	~100 (1 A g^{-1})*	90%, 1,000 cycles	0.0797*	10.22*	W:400 I:400	Photolithography and EPD
MPG[10]	PVA/H_2SO_4 (0~1 V)	0.015	0.0807 (5mV s^{-1}) 0.016 (200V s^{-1})	17.9 (5mV s^{-1}) 3.0 (200V s^{-1})	99.1%, 100,000 cycles	0.0116*	2.5	W: 210, I: 70	oxygen plasma etching via mask
GQD[11]	Na_2SO_4	0.312	0.534 (15 μA cm^{-2})	17.1 (15 μA cm^{-2})*	93.3%, 5,000 cycles	0.074	2.38*	W:230, I:200, L:10,000,	Photolithography and EPD
G-CNT[12]	1 M Na_2SO_4 (0~1 V)	15	2.2 (0.2 V s^{-1})	1.1 (0.2 V s^{-1})	-	0.32	0.16	W:150, I: 100, L: 370	Photolithography and CVD
OLC[13]	1 M Et_4NBF_4 in PC (0~3 V)	7	~1.0 (1 V s^{-1})*	1.3 (1 V s^{-1})	100%, 10,000 cycles	1.264*	1.6	W:218, I:100, L:4500	Photolithography and EPD
RGO-CNT[14]	3 M KCl (0~1 V)	<5 *	5.5 (10 mV s^{-1}) 2.8 (1 V s^{-1})	6.1 (10 mV s^{-1}) 5.0 (1 V s^{-1})	98%, 8000 cycles	0.61*	0.68	W:100, I:50	Photolithography and electrostatic spray
AC[15]	1 M Et_4NBF_4 in PC (0~2.5 V)	1~2	2.1 (1 mV s^{-1})	2.7 (1 mV s^{-1})	-	1.825*	2.34*	W:75, I:75 L:750	Ink-jet printing
LSG[16]	PVA/H_2SO_4 (0~1 V)	7.6	2.32 (16.8 mA cm^{-3})	3.05 (16.8 mA cm^{-3})	96%, 10,000 cycles	~0.456*	~0.6	W: 330, I;150, L:4800	Laser writing
LIG[17]	H_2SO_4 (0~1 V)	25	2.72 (0.2 mA cm^{-2})*	1.1 (0.2 mA cm^{-2})*	100%, 10,000 cycles	0.375*	0.15	I:300	Laser writing
B-LIG[18]	PVA/H_2SO_4 (0~1 V)	25	12.4 (0.04 mA cm^{-2})	5.0 (0.04 mA cm^{-2})	90%, 12,000 cycles	1.4*	0.56	W:1000, I:300,	Laser writing
aMP[19]	PVA/H_2SO_4 (0~1 V)	5	8.4 (0.1 V s^{-1})	12 (0.1 V s^{-1})	98%, 20,000 cycles	1.17	1.6	W:350, I:150, L:5000,	Laser etching
MDC[20]	PVA/H_2SO_4 (0~1 V)	6.9	9 (0.05 mA cm^{-2})	12.92 (0.05 mA cm^{-2})	120%, 16,000 cycles	1.25*	1.8	W:300, I:100, L:5,000	Laser etching
rGO-PEDOT/PSS[6]	PVA/H_3PO_4 (0~1 V)	11.6	22.4 (5 mV s^{-1}) 18.1 (100 mV s^{-1}) 11.5 (1V s^{-1})	19.3 (5 mV s^{-1}) 15.6 (100 mV s^{-1}) 9.95 (1V s^{-1})	84% after 20,000 cycles	3.46	2.98	W: 400, I:100, L:8000	Laser etching

		57.9	84.7 (5 mV s^{-1}) 55.9 (100 mV s^{-1}) 14.7 (1V s^{-1})	14.6 (5 mV s^{-1}) 9.63 (100 mV s^{-1}) 2.55 (1V s^{-1})	94.3% after 10,000 cycles	13.1	2.26		
PANi[21]	PVA/H_2SO_4 (0~0.8 V)	0.4	1.17 (0.1 mA cm^{-2})*	25.4 (0.1 mA cm^{-2})*	96%, 1000 cycles	0.1625*	3.53*	W:100, I:500, L:3000	Photolithography
G-PANi[22]	PVA/H_2SO_4 (0~1 V)	4.5	52.5 (10 mV s^{-1})* 20.75 (100 mV s^{-1})*	109 (10 mV s^{-1})* 43 (100 mV s^{-1})*	90%, 1,000 cycles 87%, 5,000 cycles 67 %, 10,000 cycles	7.3	15.1	W:210, I:70	oxygen plasma etching via mask
LIG-PANi[23]	PVA/H_2SO_4 (0~0.8 V)	76	90.3 (0.5 mA cm^{-2}) * 67.75 (20 mA cm^{-2}) *	11.8 (0.5 mA cm^{-2}) * 8.9 (20 mA cm^{-2}) *	97%, 6000 cycles	8	1.1	W:1000, I:300, L:4100	Laser writing and EPD
LIG-MnO_2[23]	PVA/LiCl (0~1 V)	101	233.5 (0.5 mA cm^{-2}) * 70.25 (20 mA cm^{-2})*	23.35 (0.5 mA cm^{-2}) * 7.875 (20 mA cm^{-2})*	82%, 6000 cycles	32.4	3.2		
EG-PANi[2]	1M H_2SO_4 (0~0.8V)	0.2	1.5 (10 mV s^{-1})	75 (10 mV s^{-1})	94%, 1000 cycles	0.1334	6.67	W:210, I:100, L:5500	Vacuum Filtration and Lithography
G-PANi[24]	PVA/H_2SO_4 (0~0.8 V)	2	3.31 (10 mV s^{-1}) 2.78 (200 mV s^{-1})	16.55 (10 mV s^{-1}) 13.9 (200 mV s^{-1})	85.4%, 10,000 cycles	0.302	1.51	W:~400 I:~500	Spin-coating and oxygen plasma etching
CNT-PANi[25]	PEGDA/[EMIM][TFSI] (0-1.2 V)	0.414	0.67 (5 mA cm^{-3}) 0.40 (500 mA cm^{-3})	16.1 (5 mA cm^{-3}) 9.6 (500 mA cm^{-3})	78%, 5000 cycles	0.132	3.2	W:680, I:120 L:3200	Photolithography, Spray coating, and EPD
Ppy[26]	PVA/H_2SO_4 (0~0.5 V)	0.28	8.15 (60 mV s^{-1})	291 (60 mV s^{-1})	100%, 20000 cycles	0.427	15.25	W:500, I:300, L:5000	Customized Patterning and EPD
MnO_2[27]	1 M Na_2SO_4 (0~0.8 V)	-	56.3 (27.2 µA cm^{-2})	-	72.5% , 1,000 cycles	-	-	W:3.07, I:4.03	Electron beam lighographay
LIG–FeOOH//LIG–MnO_2[23]	PVA/LiCl (0~1.8 V)	40.5	21.9 (0.25 mA cm^{-2}) 14.0 (10 mA cm^{-2})	5.4 (0.25 mA cm^{-2}) 3.456 (10 mA cm^{-2})	84%, 2000 cycles	9.6	2.4	W:1000, I:300, L:4100	Laser writing and EPD
$K_2Co_3(P_2O_7)_2 \cdot 2H_2O$//graph	PVA/KOH (0-1.07 V)	1200 nm graphene		6.0 (10mA cm^{-3})	94.4, 5000 cycles		0.96		Inkjet printing

ene[28]		and 230 nm $K_2Co_3(P_2O_7)_2 \cdot 2H_2O$							
This work	PVA/H_3PO_4 (0~0.8 V)	4.5 μm GO/PA-PE	13.8 (5 mV s^{-1}) 12.3 (100 mV s^{-1})	34.5 (5 mV s^{-1}) 30.7 (100 mV s^{-1})	70%, 5000 cycles	1.35	3.16	W:350, I:150, L:8000	Extrusion Printing
	PVA/H_3PO_4 (0~0.8 V)	80 μm GO/PA-PE	160 (5 mV s^{-1}) 90 (100 mV s^{-1})	19 (5 mV s^{-1}) 12 (100 mV s^{-1})	-	15.4	1.92		
	PVA/H_3PO_4 (0~1.2 V)	3.6 μm GO/PA-PE, G-PE asymmetric design	8.6 (5 mV s^{-1}) 7.7 (100 mV s^{-1})	25 (5 mV s^{-1}) 21 (100 mV s^{-1})	100%, 5000 cycles; 96%, 10000 cycles	1.69	4.83	W+:700, W_:350, I:150, L:8000	

[a] BNG: nitrogen and boron co-doped graphene, LSG: laser-scribed graphene , MPG: methane-plasma reduced graphene, OLC: onion-like carbon, LIG: laser-induced graphene, B-LIG: boron-doped laser-induced graphene, RGO: reduced graphene oxide, CNT: carbon nanotube, G: graphene, AC: activated carbon, aMP: activated mesophase pitch, MDC: mushroom derived carbon, PANi: polyaniline, MnO_2: manganese dioxide.

[b] and [d] based on the total projected area of the devices which includes the gaps between the electrodes.

[c] and [e] based on the total volume of the devices.

[f] W: width of microelectrode fingers, I: interspace between adjacent microelectrodes, L: the length of microelectrodes, T: thickness of film.

*Calculated based on the dimensions given in reference when specific results were not given.

References:

[1] D. Xu, Q. Xu, K. Wang, J. Chen, Z. Chen, ACS Appl. Mater. Interfaces 2013, 6, 200.

[2] Z. Liu, S. Liu, R. Dong, S. Yang, H. Lu, A. Narita, X. Feng, K. Müllen, *Small* **2017**, *13*, 1603388.

[3] X. Zhang, D. Chang, J. Liu, Y. Luo, *J. Mater. Chem.* **2010**, *20*, 5080.

[4] T. K. Ghosh, S. Gope, D. Mondal, B. Bhowmik, M. M. R. Mollick, D. Maity, I. Roy, G. Sarkar, S. Sadhukhan, D. Rana, M. Chakraborty, D. Chattopadhyay, *Int. J. Biol. Macromol.* **2014**, *66*, 338.

[5] J. Xu, K. Wang, S.-Z. Zu, B.-H. Han, Z. Wei, *ACS Nano* **2010**, *4*, 5019.

[6] Y. Liu, B. Weng, Q. Xu, Y. Hou, C. Zhao, S. Beirne, K. Shu, R. Jalili, G. G. Wallace, J. M. Razal, J. Chen, *Adv. Mater. Technol.* **2016**, *1*, 1600166.

[7] D. Antiohos, M. S. Romano, J. M. Razal, S. Beirne, P. Aitchison, A. I. Minett, G. G. Wallace, J. Chen, *J. Mater. Chem. A* **2014**, *2*, 14835.

[8] Z.-S. Wu, K. Parvez, A. Winter, H. Vieker, X. Liu, S. Han, A. Turchanin, X. Feng, K. Müllen, *Adv. Mater.* **2014**, *26*, 4552.

[9] Z. Niu, L. Zhang, L. Liu, B. Zhu, H. Dong, X. Chen, *Adv. Mater.* **2013**, *25*, 4035.

[10] Z.-S. Wu, K. Parvez, X. Feng, K. Müllen, *Nat. Commun.* **2013**, *4*, 2487.

[11] W.-W. Liu, Y.-Q. Feng, X.-B. Yan, J.-T. Chen, Q.-J. Xue, *Adv. Funct. Mater.* **2013**, *23*, 4111.

[12] J. Lin, C. Zhang, Z. Yan, Y. Zhu, Z. Peng, R. H. Hauge, D. Natelson, J. M. Tour, *Nano Lett.* **2013**, *13*, 72.

[13] D. Pech, M. Brunet, H. Durou, P. Huang, V. Mochalin, Y. Gogotsi, P.-L. Taberna, P. Simon, *Nat. Nanotechnol.* **2010**, *5*, 651.

[14] M. Beidaghi, C. Wang, *Adv. Funct. Mater.* **2012**, *22*, 4501.

[15] D. Pech, M. Brunet, P.-L. Taberna, P. Simon, N. Fabre, F. Mesnilgrente, V. Conédéra, H. Durou, *J. Power Sources* **2010**, *195*, 1266.

[16] M. F. El-Kady, R. B. Kaner, *Nat. Commun.* **2013**, *4*, 1475.

[17] J. Lin, Z. Peng, Y. Liu, F. Ruiz-Zepeda, R. Ye, E. L. G. Samuel, M. J. Yacaman, B. I. Yakobson, J. M. Tour, *Nat. Commun.* **2014**, *5*, 5714.

[18] Z. Peng, R. Ye, J. A. Mann, D. Zakhidov, Y. Li, P. R. Smalley, J. Lin, J. M. Tour, *ACS Nano* **2015**, *9*, 5868.

[19] H.-C. Huang, C.-J. Chung, C.-T. Hsieh, P.-L. Kuo, H. Teng, *Nano Energy* **2016**, *21*, 90.

[20] B. Anothumakkool, S. N. Bhange, R. Soni, S. Kurungot, *Energy Environ. Sci.* **2015**, 1339.

[21] K. Wang, W. J. Zou, B. G. Quan, A. F. Yu, H. P. Wu, P. Jiang, Z. X. Wei, *Adv. Energy Mater.* **2011**, *1*, 1068.

[22] Z. Wu, K. Parvez, S. Li, S. Yang, Z. Liu, S. Liu, X. Feng, K. Müllen, *Adv. Mater.* **2015**, *27*, 1521.

[23] L. Li, J. Zhang, Z. Peng, Y. Li, C. Gao, Y. Ji, R. Ye, N. D. Kim, Q. Zhong, Y. Yang, H. Fei, G. Ruan, J. M. Tour, *Adv. Mater.* **2016**, *28*, 838.

[24] B. Song, L. Li, Z. Lin, Z.-K. Wu, K. Moon, C.-P. Wong, *Nano Energy* **2015**, *16*, 470.

[25] J. Yun, Y. Lim, G. N. Jang, D. Kim, J. Lee, H. Park, S. Yeong, G. Lee, G. Zi, J. Sook, *Nano Energy* **2015**, *19*, 401.

[26] M. Zhu, Y. Huang, Y. Huang, H. Li, Z. Wang, Z. Pei, Q. Xue, H. Geng, C. Zhi, *Adv. Mater.* **2017**, *29*, 1605137.

[27] X. Wang, B. D. Myers, J. Yan, G. Shekhawat, V. Dravid, P. S. Lee, *Nanoscale* **2013**, *5*, 4119.

[28] H. Pang, Y. Zhang, W.-Y. Lai, Z. Hu, W. Huang, *Nano Energy* **2015**, *15*, 303.